Supporting Information

Shiraiwa et al. 10.1073/pnas.1307501110

SI Materials and Methods

KM-GAP Model and Parameters. A kinetic multi-layer model of gas-particle interactions in aerosols and clouds (KM-GAP) (1) is used for simulations. For size-resolved simulations, the bin method with full-moving size structure is used, in which the number concentration of particles in each size bin is conserved but the single particle volumes change (2). The number of size bins is 20 in this study. Coagulation is not considered in the model, as the coagulation timescale of more than a day significantly exceeds the experimental timescale (3, 4). KM-GAP consists of multiple model compartments and layers, respectively: gas phase, near-surface gas phase, sorption layer, surface layer, and a number of bulk layers. KM-GAP treats the following processes explicitly: gas-phase diffusion, gas-surface transport (reversible adsorption), surface-bulk exchange, bulk diffusion, and a selection of chemical reactions in the gas and particle phases. Note that assumptions of instantaneous gas-particle partitioning and homogeneous mixing of the particle bulk, which are often assumed in secondary organic aerosol (SOA) modeling studies (5), were not applied. Surface and bulk layers can either grow or shrink in response to mass transport, which eventually leads to particle growth or shrinkage. Surface-bulk transport and bulk diffusion are treated as mass transport from one bulk layer to the next through first-order transport velocities, which are calculated from the bulk diffusion coefficients (1). As the experiments considered here were conducted under dry conditions, ammonium sulfate is assumed to remain in the form of crystalline seed particles on which SOA condenses. The ammonium sulfate core is represented by one bulk layer, and the organic phase is resolved with 10 bulk layers. Ideal mixing is assumed within the organic phase (mole fraction-based activity coefficients are assumed to be unity), an assumption that is reasonable for an SOA phase formed by the oxidation products of a single parent compound (here dodecane) at conditions of low water content (low relative humidity) (6). Loss of gas-phase semivolatile organic compounds (SVOCs) to the chamber wall (4, 7) is considered using a pseudo-first order gas-phase wall-loss coefficient k_w (see *Gas-phase wall loss* for determination of k_w values). Particle wall loss is not considered in the model; thus, the particle-number concentration stays constant. The dynamics of mass concentrations in the gas and particle phases and of the aerosol size distribution are computed by numerically solving the ordinary differential equations for the mass balance of each model compartment (1).

Five generations of gas-phase oxidation are considered, each generation of which is represented by a surrogate compound. Yee et al. (8) have developed the dodecane low-NO_x gas-phase chemical mechanism based on gas-phase measurements of dodecane photooxidation in conjunction with the Master Chemical Mechanism (MCM, version 3.2) (9). Yee et al. (8) estimated gas-phase saturation concentrations ($\mu g \cdot m^{-3}$) over the pure (subcooled) liquids (C_i^0) for oxidation products predicted by a detailed gas-phase chemical mechanism using the EVAPORATION (Estimation of Vapor Pressure of Organics, Accounting for Temperature, Intramolecular, and Nonadditivity effects) method (10), as shown in the open color circles in Fig. 1*B*. C_i^0 values for surrogate compounds are determined by varying C_i^0 over the predicted range for each generation to fit to the measured SOA mass. The first-order gas-phase reaction rate constants are summarized in Table S1, which is based on the chemical mechanism for dodecane photooxidation developed by Yee et al. (8). Concerning the branching ratio for formation of reactive carbonyl compounds in the fourth generation of gas-phase oxidation, a number of compounds are predicted to contain ketone and aldehyde groups by the chemical mechanism (8); thus, we chose to vary the branching ratio over the range of 0.1–0.9. For the simulations presented in Fig. 1, the value of 0.4 is taken. In the multiphase scenario, particle-phase reactions between SVOCs and reactive carbonyls are considered using the second-order bulk reaction rate coefficient (k_{BR}) as listed in Table S1. k_{BR} is assumed to be the same for all reactions. The k_{BR} value was varied to fit the model to the experimental data, resulting in a value of $k_{BR} = 2 \times 10^{-20}$ $cm^3 \cdot s^{-1}$.

The required kinetic parameters for the SVOCs are listed in Table S2, which includes an estimate for the surface accommodation coefficient on a free substrate (α_s), the molecular desorption lifetime (τ_d), gas and bulk diffusion coefficients (D_g, D_b), and the second-order bulk reaction rate coefficient (k_{BR}) for the reaction of reactive carbonyl with SVOCs. D_g is assumed to be 0.05 $cm^2 \cdot s^{-1}$ (11). Note that the sensitivity studies by varying D_g in the range of 0.02–0.2 $cm^2 \cdot s^{-1}$ revealed that D_g is not critical for describing SOA mass and size distribution, indicating that gas-phase diffusion is not the limiting step in SOA formation. τ_d is assumed to be 1 μs (1). α_s is often assumed to be unity in organic aerosol modeling studies (12). Estimates of the accommodation coefficient of SVOC using thermodenuders have resulted in values in the range of 0.28–0.46 (13). α_s is estimated to be 0.3–0.5 by kinetic modeling (1) of evaporation data of dioctyl phthalate (14). In this study, we assume $\alpha_s = 0.5$. A sensitivity study by varying α_s in the range of 0.1–1 in the multiphase scenario revealed that SOA mass and size distribution are not especially sensitive to the value of α_s, suggesting that surface accommodation is not the limiting step in SOA growth in the present case.

Neither the bulk viscosity nor the bulk diffusivity of dodecane SOA is known. Saukko et al. (15) measured a bounce behavior of SOA particles formed from the oxidation of *n*-heptadecane (a long-chain alkane). At low relative humidity (RH), particles bounced from the plate of an inertial low-pressure impactor, indicating that they are not a liquid (of low viscosity), but the particles did not bounce with the behavior of solid or glassy particles; with a bounce fraction of ~0.5, the *n*-heptadecane SOA particles are deemed to be semisolid. The typical bulk diffusivities of multifunctional organic compounds in semisolid phases range from 10^{-20} to 10^{-10} $cm^2 \cdot s^{-1}$ (16, 17). We assume here that the SOA products from the *n*-dodecane oxidation have similar diffusivities as the *n*-heptadecane SOA. D_b was varied systematically over the given range to fit to the data of SOA mass and size distribution; the optimal value was found to be 10^{-12} $cm^2 \cdot s^{-1}$. Note that, if the particles are assumed to be liquid with D_b in the range of 10^{-10} to 10^{-5} $cm^2 \cdot s^{-1}$, indeed size distribution was not reproduced as well as in the case that the particle is assumed to be semisolid. The most sensitive parameters in fitting SOA mass are the gas-phase saturation concentrations ($\mu g \cdot m^{-3}$) for SVOCs. The second-order bulk reaction rate coefficient k_{BR} is the most critical parameter in controlling the evolution of the particle number size distribution. This finding is understood as this coefficient affects the average vapor pressures of the condensed SOA species via the conversion of higher-volatility monomers to low-volatility dimers and oligomers.

Dodecane Photooxidation Experiments. ***Experimental methods.*** Dodecane photooxidation experiments were conducted in the dual 28 m^3 Caltech Environmental Chambers (3, 18) as described in Yee et al.

(8). The extended OH exposure of more than 22 h was achieved using the experimental chamber protocol of Loza et al. (19). A gas chromatograph with flame ionization detection (GC-FID; Agilent 6890) with an HP-5 column was used to monitor the dodecane decay at 1 h time resolution. A chemical ionization mass spectrometer (CIMS) (20–22) was used for tracking the gas-phase development of several hydroperoxide species, ketones, and acids. The CIMS operated in both positive ionization mode for a mass scan range of 50–200 amu $[M\bullet(H_2O)_n.H]^+$ and negative ionization mode for a mass scan range of 50–300 amu $[M\bullet CF_3O]^-$, $[M\bullet F]^-$, where M is the analyte. NO, NO_x, O_3, temperature, and RH were all monitored. NO and NO_x levels remained below 5 parts per billion (ppb), the lower detection limit of the chemiluminescence analyzer (Horiba; APNA 360), and photochemical simulations (8) confirmed that, at the sufficiently low levels of NO_x, the fate of the alkylperoxy radical (RO_2) is dominated by reaction with HO_2. Initial O_3 levels were 3 ppb, rising to 22 ppb by the end of the experiment. Temperature remained between 296 and 298 K after irradiation began, and RH remained below 5%.

A differential mobility analyzer (TSI Model 3081), coupled with a condensation particle counter (TSI Model 3010), was used for monitoring the particle-size distribution. An Aerodyne high-resolution time-of-flight aerosol mass spectrometer (HR-ToF-AMS) was operated according to protocols described in Yee et al. (8) and Craven et al. (23). Briefly, the HR-ToF-AMS (24) was operated collecting data at 1 min resolution, switching between a higher resolution, lower sensitivity "W" mode and a lower resolution, higher sensitivity "V" mode. Analysis of AMS data were performed according to analysis procedures previously described (24–27). Chamber reactors were flushed for 24 h with purified dry air before each experiment. Then 280 μL of 50% by weight aqueous H_2O_2 solution was injected into a glass trap. The glass trap was submerged in a warm water bath (35–38 °C), and the solution was evaporated by flowing 5 L·min^{-1} of purified dry air through the trap into the chamber. This resulted in ∼4 ppm H_2O_2 concentration in the chamber. A 0.015 M aqueous ammonium sulfate solution was atomized into the chamber until a seed volume of ∼11 μm^3·cm^{-3} was achieved. Next, 9 μL of *n*-dodecane (Sigma-Aldrich) was injected into a glass bulb and evaporated under gentle heating into a 5 L·min^{-1} flow of purified dry air delivered to the chamber, resulting in an initial concentration of 34 ppb. After 1 h of mixing, the blacklights were turned on to initiate photooxidation.

With the same procedure, the photooxidation experiments were also conducted with an initial concentration of dodecane of 8 ppb. The AMS was not available for the 8 ppb experiments. For those experiments, the measured SOA mass and particle size distribution are modeled well using the same parameters of the multiphase scenarios for 34 ppb experiment, as shown in Fig. S3.

Particle wall loss. The upper and lower wall loss corrections bound the amount of aerosol deposited to the Fluorinated ethylene propylene (FEP) Teflon chamber walls during an experiment. To estimate the mass growth rate of wall-deposited particles, the mass growth rate of suspended particles must be determined. We use the Aerosol Parameter Estimation (APE) model described by Pierce et al. (28) for this purpose. The APE model uses the General Dynamic Equation (29) to describe the condensation, coagulation, and wall loss of an aerosol population. The model is initialized with a suspended particle-size distribution at one time step and solves for particle wall loss parameters and a mass growth parameter, F_c (cm·s^{-1}), that produce the best match to the particle size distribution measured at the next time step. In the present case, particle wall loss rate constants are determined in separate particle wall loss experiments (18, 19, 30), and these rate constants are used directly in the model.

Once the mass growth parameters are known, they are applied to particles deposited to the walls. The aerosol General Dynamic Equation also governs deposited particle size distribution behavior, and deposited particles are assumed not to undergo coagulation. The change in the size distribution for deposited particles is governed by

$$\frac{\partial n_w}{\partial t} = \beta(D_p) n_s(D_p,t) - F_c \omega \left[-\frac{1}{D_p^2} n_w(D_p,t) + \frac{1}{D_p} \frac{\partial n_w(D_p,t)}{\partial D_p} \right], \quad \textbf{[S1]}$$

where n_w is the deposited particle size distribution (cm^{-3}), t is time (s), $\beta(D_p)$ is the wall loss rate constant, D_p is the particle diameter (cm), n_s is the suspended particle size distribution (cm^{-3}), and ω is a parameter that describes the extent of gas-particle partitioning for deposited particles. Values for ω range from 0 to 1, with $\omega = 0$ representing no gas-particle partitioning to deposited particles whereas $\omega = 1$ describes gas-particle partitioning to deposited particles identical to that to suspended particles. Here, only the limits (0, 1) for values of ω are considered. To determine the deposited particle size distribution, Eq. **S1** is solved at each size distribution time step using the value of F_c calculated from the APE model at that time step with constant ω. The wall loss corrected particle-size distribution is calculated by summing the suspended and deposited number size distributions. The wall loss corrected SOA volume concentration is calculated from the wall loss corrected size distribution. To calculate the mass of organic aerosol formed, the seed particle volume concentration is subtracted from the wall loss corrected particle volume concentration, and the resulting organic volume concentration is multiplied by a mean particle density, here 1.12 g·cm^{-3}, as determined in a separate nucleation chamber experiment (seed-free), to obtain the organic mass concentration.

Gas-phase wall loss. Gas-phase SVOCs can be absorbed by the Teflon film during the experiments (4, 7). The pseudo-first order gas-phase wall loss coefficient k_w is determined from dark vapor-phase wall loss experiments. Two vapor-phase wall loss experiments were run, using 3,6-octanediol and 2-dodecanone (Sigma-Aldrich), respectively. The hydrocarbon was injected into the reactor, and then the decay was monitored by the CIMS. A first-order wall loss coefficient was calculated from the slope of ln$C$/lnC_o vs. time, where C is the signal for the hydrocarbon and C_o is the hydrocarbon signal 21 min after completion of the hydrocarbon injection (mixing time). Then 10.7 mg of 3,6-octanediol was weighed out into a glass bulb and gently heated while 5 L·min^{-1} of dry purified air flowed through to the reactor. There was slight recondensation on the injection line, leading to incomplete delivery to the reactor. The 3,6-octanediol signal dropped by 39% over 14 h, leading to a first-order fit of $k_w = 9.6 \times 10^{-6}$ s^{-1}. For the 2-dodecanone experiment, 15.5 μL of 2-dodecanone was injected to the chamber, and its signal decayed by 14% over 22 h, resulting in $k_w = 2.2 \times 10^{-6}$ s^{-1}. Due to difficulties in handling these standards for calibration on the CIMS, the suspended concentration after injection could not be verified to match the target concentration based on the injection amount. Without a calibration factor, the presence of rapid vapor-phase wall loss as observed in Matsunaga and Ziemann (7) cannot be ruled out. If this behavior occurs during the injection or mixing period before C_o is defined, the true rates should be higher than those calculated here. Therefore, we refer to the calculated k_w as pseudo-first order. If a confident calibration factor could be established on the CIMS, care would still need to be taken to minimize losses due to recondensation in the injection line so that these losses are not falsely attributed to rapid vapor-phase wall loss in the reactor.

For the KM-GAP simulations, k_w of SVOCs was varied between the measured values (2.2×10^{-6} to 9.6×10^{-6} s^{-1}) assuming that all five generations of SVOCs are characterized by

the same k_w value. It is found that the value of k_w does not affect the evolution of the shape of the size distribution but can lead to a lower modeled SOA mass up to ~30%. For the simulations of dodecane photooxidation, $k_w = 5 \times 10^{-6}$ s^{-1} is assumed.

Tridecanal Injection Experiments. ***Experimental methods.*** The tridecanal injection experiment was run in a 24 m^3 FEP teflon (2 mil) reactor. The same gas- and particle-phase instruments as described in the photooxidation experiments in *Dodecane Photooxidation Experiments, Experimental methods* were used, except that a compact-time-of-flight aerosol mass spectrometer (C-ToF-AMS) (31) was used. Injection protocols were also the same, except loadings were modified to speed up the chemical development and to achieve an organic loading sufficient for offline filter analyses [Direct analysis in real time mass spectrometry (DART-MS)]. Then 280 μL of aqueous H_2O_2 solution (50% by weight) was injected to achieve a starting concentration of ~5 ppm of H_2O_2 in the reactor. The initial *n*-dodecane concentration was 239 ppb as measured by the GC-FID. Throughout the experiment, NO_x levels remained below the lower detection limit of the analyzer, temperature ranged over 21–22.5 °C, and RH remained below 10%.

Photooxidation occurred during the first 4 h of the experiment. The remainder of the experiment was conducted in the dark. After 6 h from the start of irradiation, tridecanal (Sigma-Aldrich) was injected. Then 24.5 mg of tridecanal (assuming no line/wall losses) was delivered to the reactor by evaporating it under gentle heating into a flow of 5 L·min^{-1} of dry purified air for 30 min. Tridecanal concentration was 9.5 (± 2.5) ppb following injection, as measured by the GC-FID. Filter sampling took place after the SOA mass peaked starting at hour 9. A total sample volume of ~1.9 m^3 (2 h at 16 L·min^{-1}) was drawn onto a Teflon filter (47 mm diameter) and analyzed offline using DART-MS.

Estimation of the particle-phase reaction rate coefficient. Tridecanal reacts with SVOCs (e.g., organic hydroperoxides) to form peroxyhemiacetals (PHA) in the particle phase. Thus, the change of the bulk number concentration of PHA $[PHA]_b$ (cm^{-3}) can be described as follows:

$$\frac{d[\mathrm{PHA}]_b}{dt} = k_{BR,Tri}[\mathrm{SVOC}]_b[\mathrm{Tri}]_b, \qquad \textbf{[S2]}$$

where $k_{BR,Tri}$ (cm^3·s^{-1}) is the second-order reaction rate coefficient between tridecanal and SVOCs. As the increase of the total particle mass concentration C_{tot} (μg·m^{-3}) is predicted to be dominated by PHA formation in the present study, its rate of change can be described using the particle mass concentration of PHA C_{PHA}^{PM} (μg·m^{-3} of air):

$$\frac{dC_{tot}}{dt} \approx \frac{dC_{PHA}^{PM}}{dt} = \frac{M_{PHA}}{N_A}\left(10^6 \mu g\ g^{-1}\right)\frac{d[\mathrm{PHA}]_b}{dt} = \frac{M_{PHA}}{N_A}\left(10^6 \mu g\ g^{-1}\right)k_{BR,Tri}[\mathrm{SVOC}]_b[\mathrm{Tri}]_b, \qquad \textbf{[S3]}$$

where M_{PHA} is the molar mass of PHA (~300–400 g·mol^{-1}) and N_A is the Avogadro constant (6.02×10^{23} mol^{-1}). The factor 10^6 is for the unit conversion of g to μg. The average bulk number concentration $[Tri]_b$ (cm^{-3}) and the average particle-phase mass concentration of tridecanal C_{Tri}^{PM} (μg·m^{-3}) can be roughly estimated based on equilibrium gas-particle partitioning theory (32, 33) using its volatility, namely the pure component gas-phase saturation concentration $C_{Tri}^{0} = 1.6 \times 10^5$ μg·m^{-3} (34),

$$[\mathrm{Tri}]_b = \frac{C_{Tri}^{PM}}{M_{Tri}/N_A}\left(10^6 \mu g\ g^{-1}\right) \qquad \textbf{[S4]}$$

$$C_{Tri}^{PM} = \frac{C_{Tri}^{g}}{C_{Tri}^{0}}C_{tot}, \qquad \textbf{[S5]}$$

where M_{Tri} is the molar mass of tridecanal (198 g·mol^{-1}) and C_{Tri}^{g} (μg·m^{-3}) is the gas phase mass concentration of tridecanal. Note that this is an approximation as a concentration gradient can exist due to slow bulk diffusion. The initial tridecanal gas-phase number concentration was measured by the CIMS to be 9.5 (±2.5) ppb, which corresponds to C_{Tri}^{g} = 77 (±20) μg·m^{-3}. $[SVOC]_b$ can be estimated assuming an average molar mass of SVOC (~200–300 g·mol^{-1}), and a certain fraction (10–100%) of the organic particle content is reactive toward aldehydes, resulting in $[SVOC]_b \sim 10^{20}$ to 10^{21} cm^{-3}.

Based on Eq. **S3**, dC_{tot}/dt is constant if $[SVOC]_b$ and $[Tri]_b$ are constant. Indeed, C_{tot} increased linearly from 22 μg·m^{-3} at tridecanal injection at 6 h to 61 μg·m^{-3} at 6.7 h (Fig. 4 of the main text), corresponding to dC_{tot}/dt = 0.017 μg·m^{-3}·s^{-1}. Inserting these values in Eq. **S3**, $k_{BR,Tri}$ can be estimated to be 2×10^{-22} to 2×10^{-20} cm^3·s^{-1} (or 0.12–12 M^{-1}·s^{-1}). This value is in good agreement with the second-order reaction rate coefficient between reactive carbonyl and SVOCs (k_{BR}) estimated by KM-GAP (12 M^{-1}·s^{-1}) in simulating dodecane photooxidation in which different aldehydes and ketones may be relevant reactants.

DART-MS Analysis. Duplicate Teflon filters (PALL Life Sciences; 47 mm diameter, 1.0 μm pore size, Teflon membrane) were used for particle collection from the chamber upon stabilization of the aerosol volume for off-line chemical analysis. Chamber air was pulled through two stainless steel filter assemblies containing two filters for 2 h at rates of 16 and 23 L·min^{-1}, respectively. In the standard chamber filter collection procedure, the upstream filter collected particles, and the downstream filter served to indicate whether breakthrough had occurred or whether gaseous compounds were condensing on the filters. Upon the termination of the collection period, the filters were removed from the assembly with precleaned stainless steel forceps and stored in 20-mL glass vials with Teflon caps, which were sealed with Teflon tape and stored in plastic containers in a freezer maintained at a temperature of −20 °C.

Filters were analyzed by direct analysis in real-time mass spectrometry (DART-MS) using a custom-built DART source (J. L. Beauchamp group, Caltech) interfaced to a Thermo LTQ ion trap mass spectrometer; positive mode ionization was used in this analysis. DART-MS is an ambient ionization method originally developed by Cody et al. (35). It achieves positive ionization through the generation of metastable triplet helium and its reaction with atmospheric water. For the final proton transfer step to occur, the analyte's proton affinity must exceed that of water. SOA samples collected on Teflon filters were analyzed by folding the filter in half with clean stainless steel forceps, and placing the folded filter so the DART stream ablated the aerosol-containing edge. Blank filters and the breakthrough test filters were analyzed as experimental controls. Data were analyzed using the Thermo proprietary software program, Xcalibur.

SOA samples were also extracted in a 1:1 mixture of GC grade heptane and acetone (vol/vol) via sonication. The extracts were dried down by a gentle stream of N_2, then reconstituted in 150 μL of 1:1 mixture of GC grade heptane and acetone (vol/vol) for analysis by GC/MS (Varian Saturn 2200) with a programmed temperature vaporization (PTV) inlet, DB-5MS-UI column (30 m, 0.250 mm, 0.25 μm; Agilent), and electron impact ionization and chemical ionization with methanol. The PTV temperature program was as follows: (*i*) 45 °C, 0.5 min hold; (*ii*) 180 °C min^{-1} ramp to 300 °C; and (*iii*) 300 °C, 46.58 min hold. The oven temperature program was as follows: (*i*) 65 °C, 10 min hold; (*ii*) 10 °C min^{-1} ramp to 300 °C; and (*iii*) 300 °C, 15 min hold.

Table S3 lists major peaks, defined by signal intensity > 5,000 counts for m/z < 400 Da; signal intensity > 1,000 counts for m/z > 400 Da. Proposed formulae are listed for the ions; matches were assigned when the theoretical mass was within 5 mDa of the measured mass. This mass spectrum was acquired using the AccuToF DART-MS, which was mass-calibrated in positive mode by using PEG-600. The ions with m/z above 400 Da that contain nitrogen may be assigned in two ways: (*i*) they may be nitrate-containing compounds, resulting from reaction with the background levels of NO_x in the chamber (<5 ppb); or (*ii*) they may be PHAs or contain peroxide groups, both of which form adducts with ammonia present in trace amounts in laboratory air, and are measured by DART-MS as ammonium adducts ($[M+17]^+$). The low level of NO_x and the lack of smaller mass organonitrates or alcohols suggest that the ammonium adduct option is more likely in this case.

The mass spectra in Fig. S5 were acquired using the experimental DART source in conjuction with the Thermo LTQ ion trap mass spectrometer with unit mass resolution. Fig. S5*A* shows a duplicate sample of dodecane SOA; the significant overlap with the data in Table S3 indicates similar performance across DART ion sources. Fig. S5*B* shows a sample of SOA from the dodecane low-NO_x photooxidation experiment where tridecanal was added in the gas phase to attempt to force oligomerization by PHA formation. The high-resolution AccuToF DART was unavailable for use at the time of the tridecanal experiment, so only unit mass resolution data were obtained for this sample. From Fig. S5*B*, one can observe that different high molecular weight species were formed in the tridecanal experiment, and that the added SOA mass was not simply tridecanal condensing onto the particles (i.e., the spectrum is not dominated by m/z 199), so it must have reacted after uptake.

Fig. S6 is an extracted ion chromatogram (EIC) that compares the m/z 183 signal from the heptane/acetone extracted SOA generated in the tridecanal experiment and in the dodecane photooxidation experiment. The mass loadings for each experiment were different; more mass was on the filter for the dodecane experiment than the tridecanal experiment. The m/z 183 is the AMS tracer for PHA; because the GC/MS was run in EI mode, it has the potential to generate similar ions as the AMS. Fig. S6 demonstrates that, in the tridecanal experiment, different m/z 183-producing compounds (presumably PHA) were generated. There is more variety of m/z 183-producing compounds in the dodecane experiment EIC than in the tridecanal experiment EIC; this observation suggests that the addition of tridecanal drove the oligomer-forming reaction toward a few specific products, creating less diversity than in the dodecane experiment.

1. Shiraiwa M, Pfrang C, Koop T, Pöschl U (2012) Kinetic multi-layer model of gas-particle interactions in aerosols and clouds (KM-GAP): Linking condensation, evaporation and chemical reactions of organics, oxidants and water. *Atmos Chem Phys* 12(5):2777–2794.
2. Jacobson MZ (2005) *Fundamentals of Atmospheric Modeling* (Cambridge Univ. Press, Cambridge), 2nd Ed.
3. Cocker DR, 3rd, Flagan RC, Seinfeld JH (2001) State-of-the-art chamber facility for studying atmospheric aerosol chemistry. *Environ Sci Technol* 35(12):2594–2601.
4. Loza CL, et al. (2010) Characterization of vapor wall loss in laboratory chambers. *Environ Sci Technol* 44(13):5074–5078.
5. Hallquist M, et al. (2009) The formation, properties and impact of secondary organic aerosol: Current and emerging issues. *Atmos Chem Phys* 9(14):5155–5235.
6. Zuend A, Seinfeld JH (2012) Modeling the gas-particle partitioning of secondary organic aerosol: The importance of liquid-liquid phase separation. *Atmos Chem Phys* 12(9):3857–3882.
7. Matsunaga A, Ziemann PJ (2010) Gas-wall partitioning of organic compounds in a Teflon film chamber and potential effects on reaction product and aerosol yield measurements. *Aerosol Sci Technol* 44(10):881–892.
8. Yee LD, et al. (2012) Secondary organic aerosol formation from low-NO_x photooxidation of dodecane: Evolution of multigeneration gas-phase chemistry and aerosol composition. *J Phys Chem A* 116(24):6211–6230.
9. Saunders SM, Jenkin ME, Derwent RG, Pilling MJ (2003) Protocol for the development of the Master Chemical Mechanism, MCM v3 (Part A): Tropospheric degradation of non-aromatic volatile organic compounds. *Atmos Chem Phys* 3(1):161–180.
10. Compernolle S, Ceulemans K, Muller JF (2011) EVAPORATION: A new vapour pressure estimation methodfor organic molecules including non-additivity and intramolecular interactions. *Atmos Chem Phys* 11(18):9431–9450.
11. Bilde M, Svenningsson B, Monster J, Rosenorn T (2003) Even-odd alternation of evaporation rates and vapor pressures of C3-C9 dicarboxylic acid aerosols. *Environ Sci Technol* 37(7):1371–1378.
12. Riipinen I, et al. (2011) Organic condensation: A vital link connecting aerosol formation to cloud condensation nuclei (CCN) concentrations. *Atmos Chem Phys* 11(8):3865–3878.
13. Saleh R, Khlystov A, Shihadeh A (2012) Determination of evaporation coefficients of ambient and laboratory-generated semivolatile organic aerosols from phase equilibration kinetics in a thermodenuder. *Aerosol Sci Technol* 46(1):22–30.
14. Vaden TD, Imre D, Beránek J, Shrivastava M, Zelenyuk A (2011) Evaporation kinetics and phase of laboratory and ambient secondary organic aerosol. *Proc Natl Acad Sci USA* 108(6):2190–2195.
15. Saukko E, et al. (2012) Humidity-dependent phase state of SOA particles from biogenic and anthropogenic precursors. *Atmos Chem Phys* 12(16):7517–7529.
16. Mikhailov E, Vlasenko S, Martin ST, Koop T, Pöschl U (2009) Amorphous and crystalline aerosol particles interacting with water vapor: Conceptual framework and experimental evidence for restructuring, phase transitions and kinetic limitations. *Atmos Chem Phys* 9(2):9491–9522.
17. Shiraiwa M, Ammann M, Koop T, Pöschl U (2011) Gas uptake and chemical aging of semisolid organic aerosol particles. *Proc Natl Acad Sci USA* 108(27):11003–11008.
18. Keywood MD, Varutbangkul V, Bahreini R, Flagan RC, Seinfeld JH (2004) Secondary organic aerosol formation from the ozonolysis of cycloalkenes and related compounds. *Environ Sci Technol* 38(15):4157–4164.
19. Loza CL, et al. (2012) Chemical aging of m-xylene secondary organic aerosol: Laboratory chamber study. *Atmos Chem Phys* 12(1):151–167.
20. Paulot F, et al. (2009) Isoprene photooxidation: New insights into the production of acids and organic nitrates. *Atmos Chem Phys* 9(4):1479–1501.
21. St Clair JM, McCabe DC, Crounse JD, Steiner U, Wennberg PO (2010) Chemical ionization tandem mass spectrometer for the in situ measurement of methyl hydrogen peroxide. *Rev Sci Instrum* 81(9):094102–094106.
22. Crounse JD, Paulot F, Kjaergaard HG, Wennberg PO (2011) Peroxy radical isomerization in the oxidation of isoprene. *Phys Chem Chem Phys* 13(30):13607–13613.
23. Craven JS, et al. (2012) Analysis of secondary organic aerosol formation and aging using positive matrix factorization of high-resolution aerosol mass spectra: Application to the dodecane low-NOx system. *Atmos Chem Phys* 12(24):11795–11817.
24. DeCarlo PF, et al. (2006) Field-deployable, high-resolution, time-of-flight aerosol mass spectrometer. *Anal Chem* 78(24):8281–8289.
25. Allan JD, et al. (2004) A generalised method for the extraction of chemically resolved mass spectra from Aerodyne aerosol mass spectrometer data. *J Aerosol Sci* 35(7): 909–922.
26. Aiken AC, DeCarlo PF, Jimenez JL (2007) Elemental analysis of organic species with electron ionization high-resolution mass spectrometry. *Anal Chem* 79(21):8350–8358.
27. Aiken AC, et al. (2008) O/C and OM/OC ratios of primary, secondary, and ambient organic aerosols with high-resolution time-of-flight aerosol mass spectrometry. *Environ Sci Technol* 42(12):4478–4485.
28. Pierce JR, et al. (2008) Constraining particle evolution from wall losses, coagulation, and condensation-evaporation in smog-chamber experiments: Optimal estimation based on size distribution measurements. *Aerosol Sci Technol* 42(12):1001–1015.
29. Seinfeld JH, Pandis SN (2006) *Atmospheric Chemistry and Physics: From Air Pollution to Climate Change* (Wiley, New York).
30. Ng NL, et al. (2007) Secondary organic aerosol formation from m-xylene, toluene, and benzene. *Atmos Chem Phys* 7(14):3909–3922.
31. Drewnick F, et al. (2005) A new time-of-flight aerosol mass spectrometer (TOF-AMS): Instrument description and first field deployment. *Aerosol Sci Technol* 39(7):637–658.
32. Pankow JF (1994) An absorption model of gas-particle partitioning of organic-compounds in the atmosphere. *Atmos Environ* 28(2):185–188.
33. Donahue NM, Robinson AL, Stanier CO, Pandis SN (2006) Coupled partitioning, dilution, and chemical aging of semivolatile organics. *Environ Sci Technol* 40(8): 2635–2643.
34. Weast RC (1982) *Handbook of Chemistry and Physics* (CRC, Boca Raton, FL).
35. Cody RB, Laramée JA, Durst HD (2005) Versatile new ion source for the analysis of materials in open air under ambient conditions. *Anal Chem* 77(8):2297–2302.

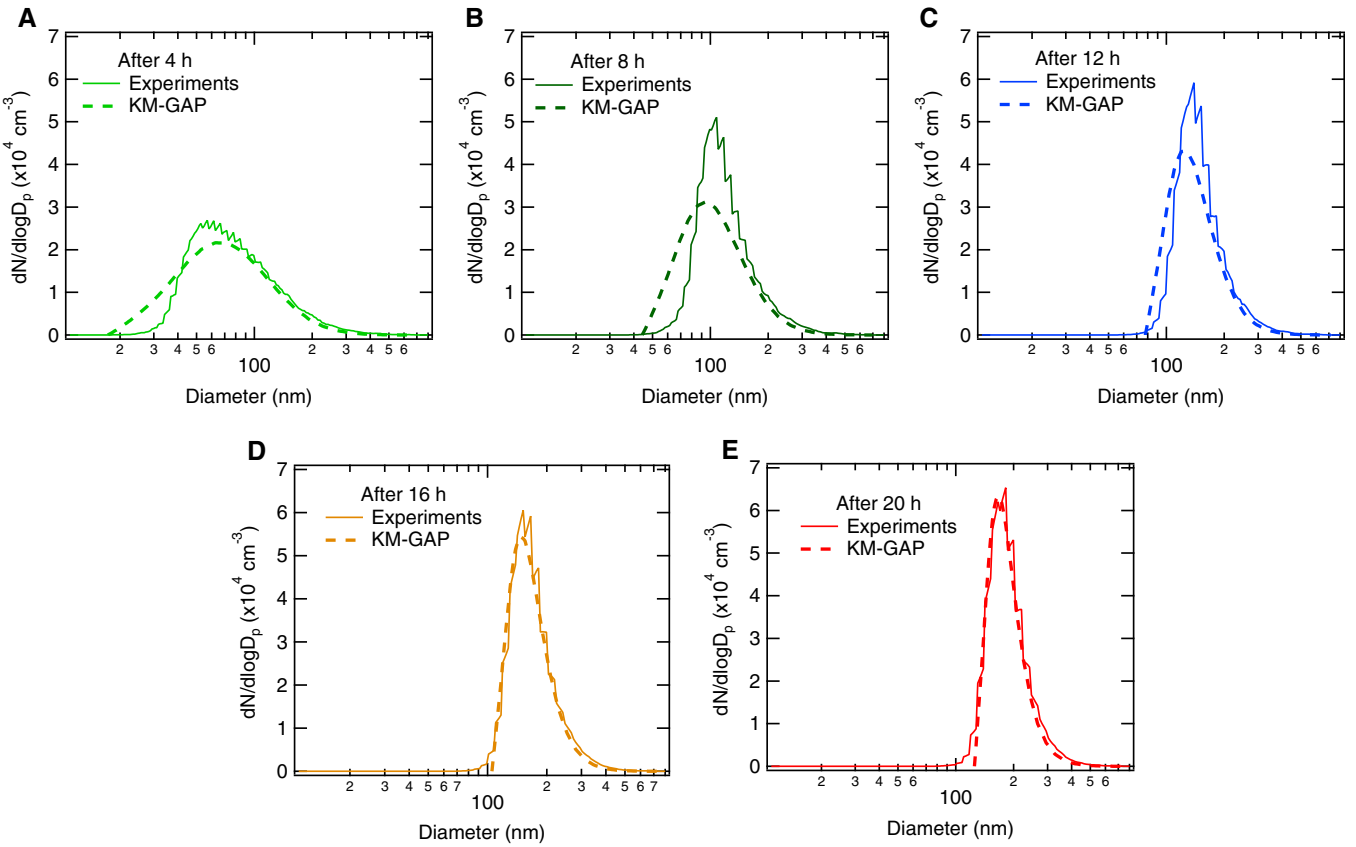

Fig. S1. Experimental (with the upper-bound wall loss correction) and modeled number size distribution (dN/dlogD) by KM-GAP with the multiphase scenario after (*A*) 4 h, (*B*) 8 h, (*C*) 12 h, (*D*) 16 h, and (*E*) 20 h.

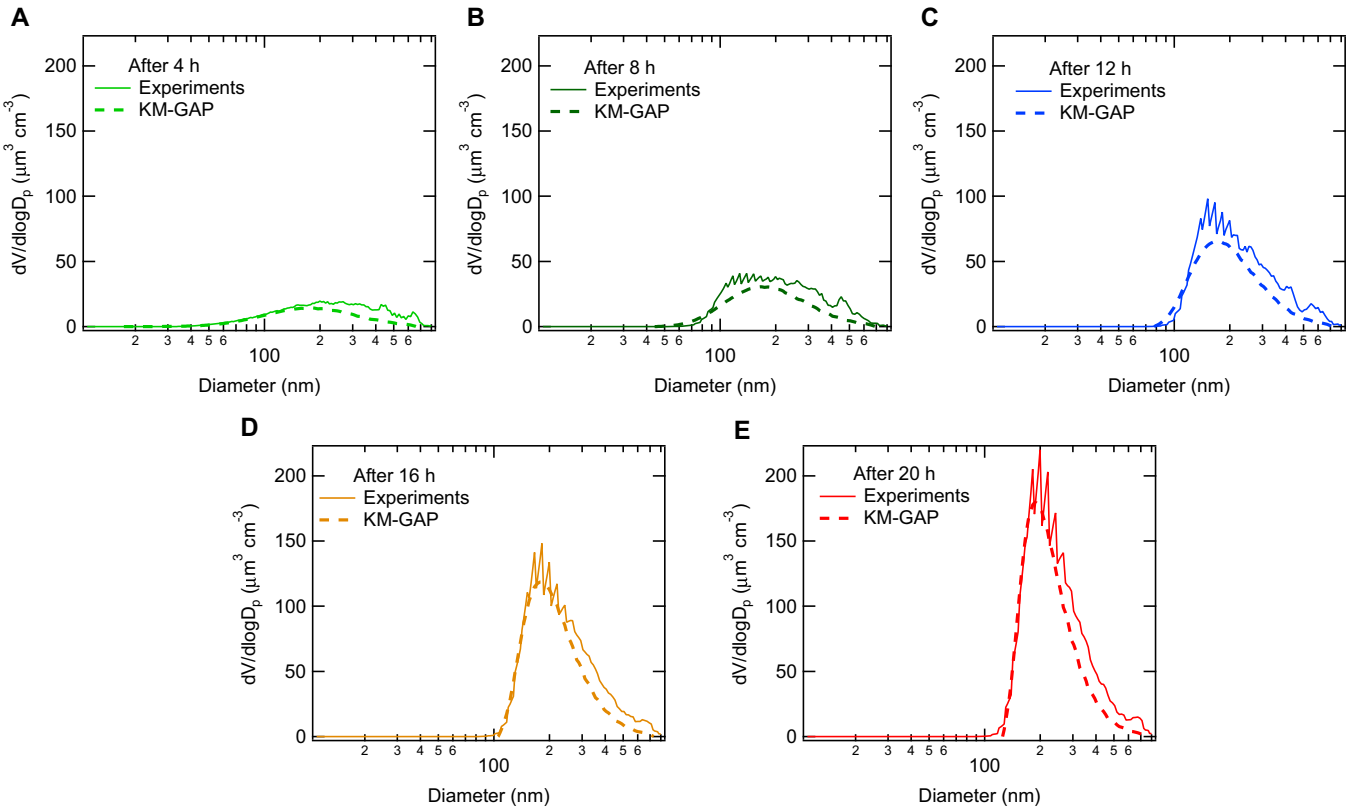

Fig. S2. Experimental (with the upper-bound wall loss correction) and modeled volume size distribution (dV/dlogD) by KM-GAP with the multiphase scenario after (*A*) 4 h, (*B*) 8 h, (*C*) 12 h, (*D*) 16 h, and (*E*) 20 h.

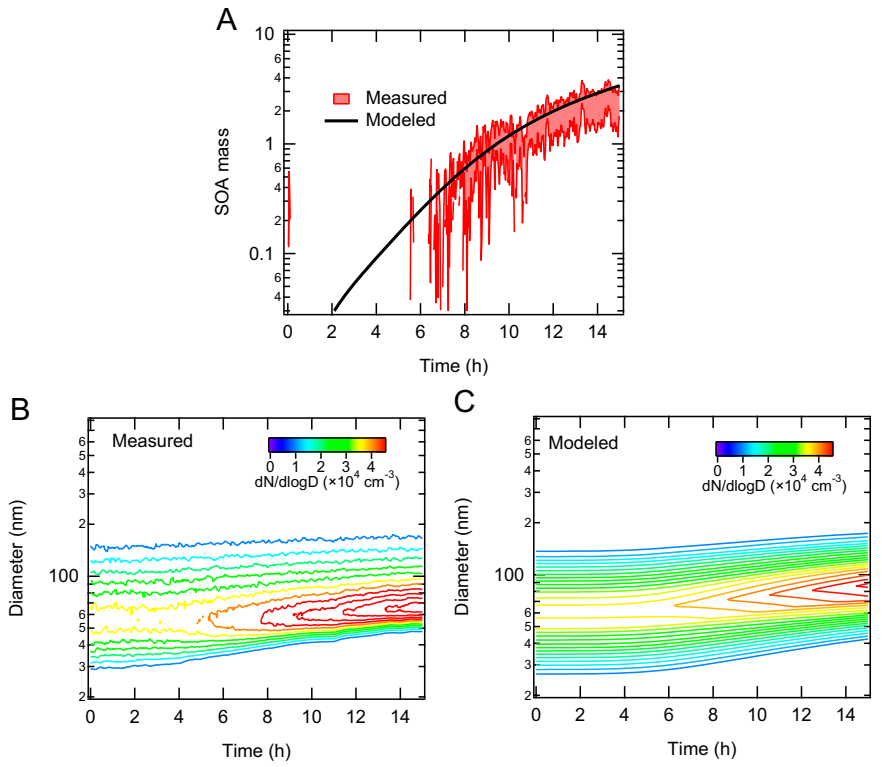

Fig. S3. Modeling SOA formation from dodecane photooxidation. Initial concentration of dodecane was 8 ppb. SOA mass and size distribution is simulated by KM-GAP using the same kinetic parameters of the multiphase scenario used for modeling photooxidation of 34 ppb dodecane (Tables S1 and S2). (*A*) Measured and modeled SOA mass. The extent of the red lines corresponds to upper and lower bound wall loss corrections. (*B*) Measured particle number size distribution with upper-bound wall loss correction. (*C*) Modeled particle number size distribution.

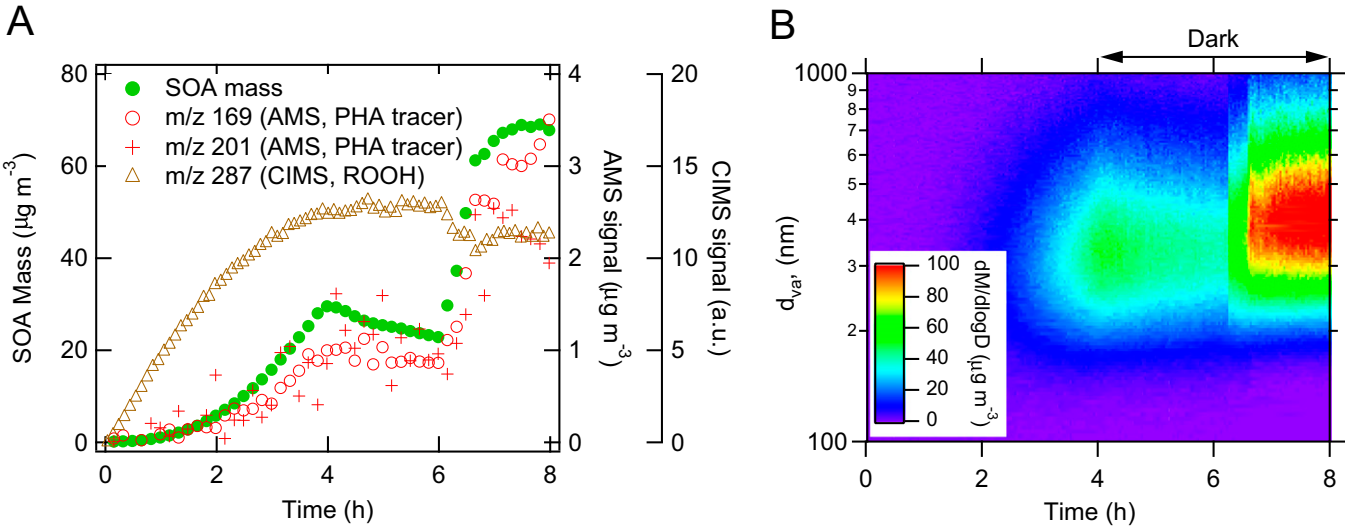

Fig. S4. Intentional aldehyde (tridecanal) injection experiments. Lights are switched off after 4 h, resulting in a net loss of SOA mass due to chamber wall deposition. After 6 h, tridecanal is injected to the chamber. (*A*) SOA mass, organic hydroperoxide ROOH ($C_{12}H_{26}O_2$) signal monitored by CIMS at *m/z* 287 and *m/z* 169 and *m/z* 201 ions measured by the C-ToF-AMS, which are tracers for ROOH-derived PHA. (*B*) Organic aerosol mass size distribution measured by the C-ToF-AMS, showing the growth of mean particle diameter from ~300 nm to ~400 nm due to tridecanal injection.

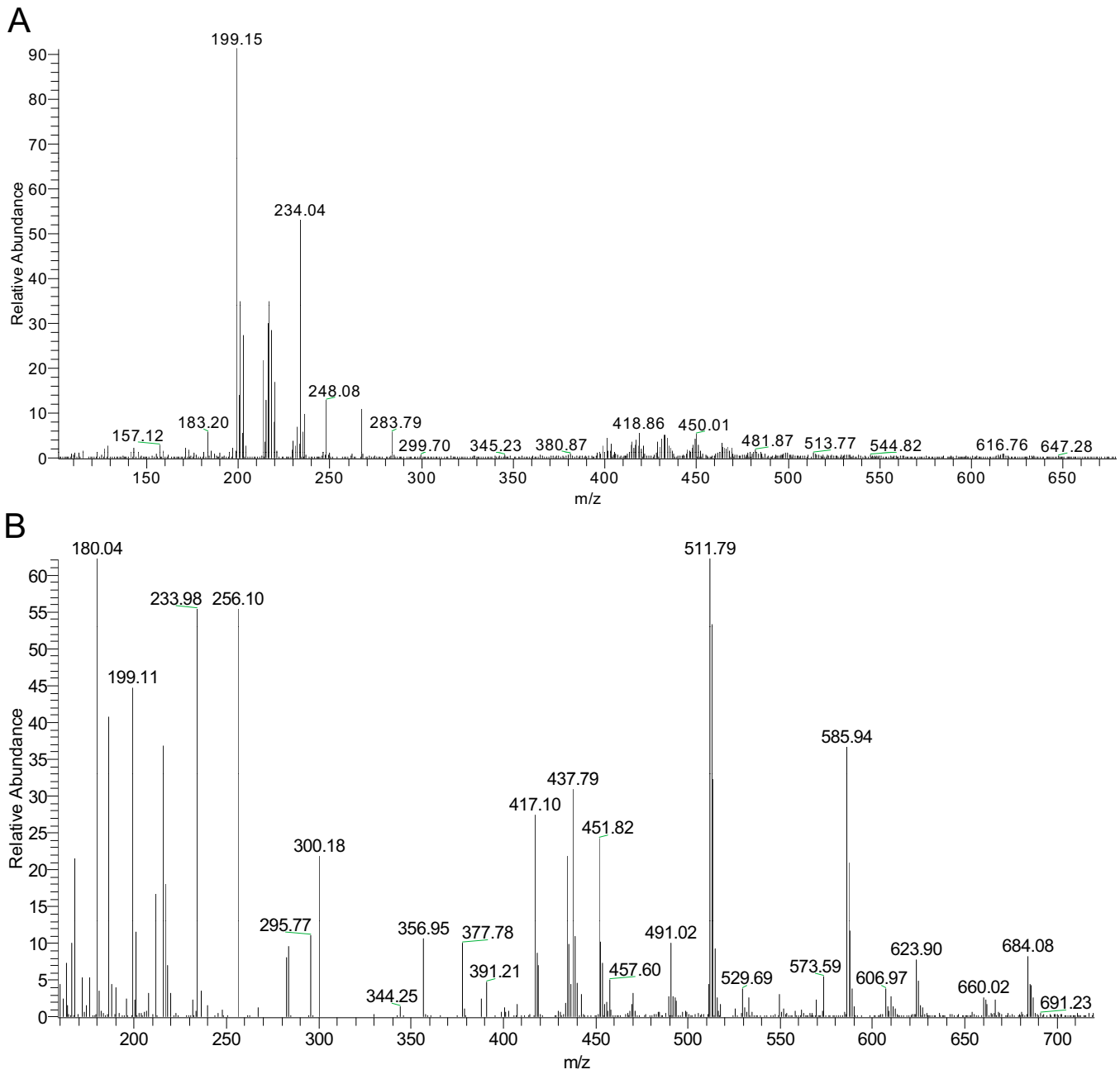

Fig. S5. DART-MS spectrum of SOA formed by photooxidation of dodecane (*A*) and that of SOA formed in tridecanal injection experiments (*B*).

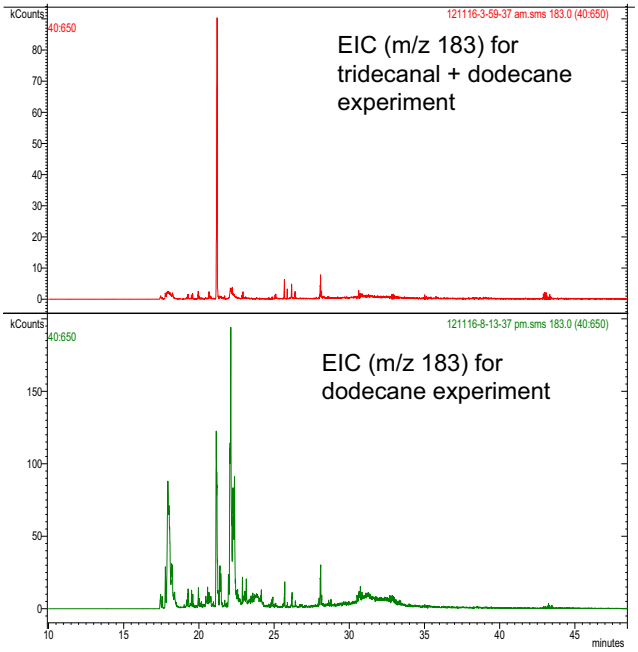

Fig. S6. Extracted ion chromatogram (EIC) that compares the *m/z* 183 signal from the heptane/acetone extracted SOA generated in the tridecanal experiment (*Upper*) and in the dodecane photooxidation experiment (*Lower*).

Table S1. Gas-phase and particle-phase chemistry considered in KM-GAP

Reaction	Reaction rate coefficient
Gas phase	
dodecane → SVOC-1	2.64×10^{-5} s^{-1}
SVOC-1→ SVOC-2	1.71×10^{-5} s^{-1}
SVOC-2→ SVOC-3	1.32×10^{-4} s^{-1}
SVOC-3→ (1 - β) SVOC-4 + β reactive carbonyl	1.85×10^{-4} s^{-1}
SVOC-4→ SVOC-5	1.85×10^{-4} s^{-1}
Particle phase	
SVOC-1 + reactive carbonyl → low volatility products	2×10^{-20} $cm^3 \cdot s^{-1}$
SVOC-2 + reactive carbonyl → low volatility products	2×10^{-20} $cm^3 \cdot s^{-1}$
SVOC-3 + reactive carbonyl → low volatility products	2×10^{-20} $cm^3 \cdot s^{-1}$
SVOC-4 + reactive carbonyl → low volatility products	2×10^{-20} $cm^3 \cdot s^{-1}$
SVOC-5 + reactive carbonyl → low volatility products	2×10^{-20} $cm^3 \cdot s^{-1}$

Gas-phase reactions are considered using the first-order conversion rate coefficients. In the multiphase scenario, particle-phase reactions are considered using the second-order reaction rate coefficient.

Table S2. Estimated kinetic parameters for the surrogate SVOCs in the KM-GAP simulations

Parameters	Description	Value
$\alpha_{s,0}$	Surface accommodation coefficient on a free substrate	0.5
τ_d	Desorption lifetime	1 μs
D_b	Bulk diffusion coefficient	10^{-12} $cm^2 \cdot s^{-1}$
D_g	Gas diffusion coefficient	0.05 $cm^2 \cdot s^{-1}$

Table S3. Major peaks in DART mass spectrum for dodecane low-NO_x SOA

m/z, Da	Intensity, counts	Proposed formula
127.15	6,253.34	$C_8H_{15}O^+$
141.16	9,527.53	$C_9H_{17}O^+$
155.17	9,916.25	$C_{10}H_{19}O^+$
183.19	10,1521.10	$C_{12}H_{23}O^+$
197.16	69,729.89	$C_{12}H_{21}O_2^+$
199.18	52,161.82	$C_{12}H_{23}O_2^+$
213.15	26,890.18	$C_{12}H_{21}O_3^+$
401.36	36,11.87	$C_{24}H_{49}O_4^+$
416.37	3,794.30	$C_{24}H_{50}O_4N^+$
430.35	4,076.51	$C_{24}H_{48}O_4N^+$
446.35	2,134.07	$C_{24}H_{48}O_6N^+$
460.34	1,223.03	$C_{24}H_{46}O_7N^+$